

Natural protein engineering in the Ω -loop: the role of Y221 in ceftazidime and ceftolozane resistance in *Pseudomonas*-derived cephalosporinase

Andrew R. Mack,^{a,b,*} Vijay Kumar,^{c,*} Magdalena A. Taracila,^{d,b} Maria F. Mojica,^{a,c} Margaret O'Shea,^b William Schinabeck,^b Galen Silver,^b Andrea M Hujer,^{d,b} Krisztina M. Papp-Wallace,^{b,d,c,†} Shuang Chen,^f Shozeb Haider,^{f,g} Emilia Caselli,^h Fabio Prati,^h Focco van den Akker,^{c,#} Robert A. Bonomo^{d,i,a,c,j,k,e,#}

^aDepartment of Molecular Biology and Microbiology, Case Western Reserve University School of Medicine, Cleveland, OH, USA

^bResearch Service, VA Northeast Healthcare System, Cleveland, OH, USA

^cDepartment of Biochemistry, Case Western Reserve University School of Medicine, Cleveland, OH, USA

^dDepartment of Medicine, Case Western Reserve University School of Medicine, Cleveland, OH, USA

^eCWRU-Cleveland VAMC Center for Antimicrobial Resistance and Epidemiology (Case VA CARES) Cleveland, OH, USA

^fDepartment of Pharmaceutical and Biological Chemistry, School of Pharmacy, University College London, London, United Kingdom

[§]UCL Centre for Advanced Research Computing, University College London, London, United Kingdom

^hDepartment of Life Sciences, University of Modena and Reggio Emilia, Modena, Italy

ⁱDepartment of Pharmacology, Case Western Reserve University School of Medicine, Cleveland, OH, USA

^jDepartment of Proteomics and Bioinformatics, Case Western Reserve University School of Medicine, Cleveland, OH, USA

^kClinician Scientist Investigator, Louis Stokes Cleveland Department of Veterans Affairs Medical Center, Cleveland, OH, USA

* Andrew Mack and Vijay Kumar contributed equally to this work. Author order was determined in order of increasing seniority.

† Present address: JMI Laboratories, a subsidiary of Element Materials Technology, North Liberty, IA, USA.

Address correspondence to Focco van den Akker (fxv5@case.edu) or Robert Bonomo (Robert.Bonomo@va.gov)

Running Title (52 of 54): Role of Y221 in ceftolozane & ceftazidime resistance

Abstract

A wide variety of clinically observed single amino acid substitutions in the Ω -loop region have been associated with increased minimum inhibitory concentrations (MICs) and resistance to ceftazidime (CAZ) and ceftolozane (TOL) in *Pseudomonas*-derived cephalosporinase and other class C β -lactamases. Herein, we demonstrate the naturally occurring tyrosine to histidine substitution of amino acid 221 (Y221H) in PDC enables CAZ and TOL hydrolysis, leading to similar kinetic profiles ($k_{\text{cat}} = 2.3 \pm 0.2 \mu\text{M}$ and $2.6 \pm 0.1 \mu\text{M}$ respectively). Mass spectrometry of PDC-3 establishes the formation of stable adducts consistent with formation of an acyl enzyme complex while spectra of E219K (a well characterized, CAZ and TOL resistant comparator) and Y221H are consistent with more rapid turnover. Thermal denaturation experiments reveal decreased stability of the variants. Importantly, PDC-3, E219K, and Y221H are all inhibited by avibactam and the boronic acid transition state inhibitors (BATSI) LP06 and S02030 with nanomolar IC_{50} values and the BATSIs stabilize all three enzymes. Crystal structures of PDC-3 and Y221H as apo enzymes and complexed with LP06 and S02030 (1.35 – 2.10 Å resolution) demonstrate ligand induced conformational changes, including a significant shift in the position of the sidechain of residue 221 in Y221H (as predicted by enhanced sampling well-tempered metadynamics simulations), and extensive hydrogen bonding between the enzymes and BATSI. The shift of residue 221 leads to the expansion of the active site pocket and molecular docking suggests substrates orientate differently and make different intermolecular interactions in the enlarged active site compared to the wild-type enzyme.

Introduction

Since the early 20th century, antibiotics have been used to prevent and treat infections. Unfortunately, during the last several decades, antimicrobial resistance (AMR) has rapidly emerged and drastically reduced our therapeutic arsenal to combat serious bacterial infections (1). Overuse of β -lactams, the most widely used class of antibiotics in the United States (2), has led to the emergence of many AMR mechanisms in pathogens that now require novel treatment strategies (3). Among the more concerning pathogens is *Pseudomonas aeruginosa*, which possesses a wide array of both intrinsic and acquired resistance mechanisms (4). Some multidrug-resistant (MDR) *P. aeruginosa* strains are resistant to nearly all antibiotics, including cephalosporins and carbapenems, important members of the β -lactam family (5). This unwelcome observation has led the Centers for Disease Control and Prevention to classify MDR *P. aeruginosa* as a “serious” threat pathogen, with an estimated 32,600 nosocomial infections leading to 2,700 deaths and \$767 million in associated healthcare costs annually (6).

The β -lactams function through covalent binding of the β -lactam ring to the active site serine of bacterial penicillin binding proteins (PBPs), a family of DD-transpeptidases involved the final crosslinking steps of peptidoglycan cell wall biosynthesis (2, 7). By inhibiting PBPs, β -lactam antibiotics disrupt cell wall biosynthesis, depleting essential precursors and ultimately killing the bacteria (8). One of the primary mechanisms of resistance to β -lactam antibiotics is the expression of β -lactamases (9), a group of bacterial enzymes that hydrolyze the β -lactam bond, rendering it ineffective. β -Lactamases are grouped into four classes (A, B, C and D) based on their mechanism (serine or metal ion based), amino acid sequence, and conserved motifs (10). All four classes of β -lactamases have been identified in *P. aeruginosa*, and the most widespread of these is the

chromosomally encoded class C β -lactamase *Pseudomonas*-derived cephalosporinase (PDC), which is often responsible for high-level resistance to β -lactam antibiotics (11–13). PDCs can provide intrinsically intermediate or resistant phenotypes to many β -lactams, including penicillins, narrow spectrum cephalosporins (including cephalothin and cephaloridine), and some expanded spectrum cephalosporins (cefotaxime) (11, 14–16). In addition, the derepression and subsequent overexpression of PDC caused by mutations in regulatory genes such as *ampD*, *ampR*, and *dacB* (PBP4) is an important mechanism of resistance to penicillins and cephalosporins (17–20). Concerningly, PDC can harbor even single amino acid substitutions resulting in expanded-spectrum cephalosporinases with activity against otherwise effective antipseudomonal cephalosporins including ceftazidime (CAZ), ceftolozane (TOL), and cefepime (FEP) (11, 16). TOL, one of the more recently developed cephalosporins, (**Figure 1A**) was mechanistically designed to improve on the chemical properties of CAZ, (**Figure 1A**) while increasing membrane permeability and taking advantage of steric effects to increase stability against class C β -lactamases (21). As a result, PDC-1 demonstrates a 20-fold higher K_M and 20-fold lower k_{cat}/K_M (catalytic efficiency) for TOL compared to CAZ (22). Unfortunately, TOL resistance quickly emerged and a wide variety of PDC variants (as well as non-PDC-mediated mechanisms) have been associated with TOL resistance (16, 23). Rates of ceftolozane-tazobactam (C/T) and ceftazidime-avibactam (CZA) resistance in the US range from 3.6% and 5.6%, respectively, among all *P. aeruginosa* isolates to as high as 30.2% and 55.0% for difficult-to-treat resistant isolates (24), only underscoring the importance of resistance against these essential antibiotics.

To combat β -lactamase-mediated resistance, β -lactams are co-administered with β -lactamase inhibitors (23, 25). Unfortunately, clinically observed PDCs (such as PDC-79 containing the E219K substitution) can cause resistance to β -lactam/ β -lactamase inhibitor

combinations (11, 16). Furthermore, the expression of PDCs can be induced by some β -lactams targeting specific penicillin-binding proteins (PBPs), thus allowing the pathogen to more readily degrade β -lactam antibiotics (26). Therefore, obtaining both a mechanistic understanding of how PDC variants recognize and hydrolyze β -lactams as well as probing how PDCs can be inhibited is an active field of study to combat this key *Pseudomonal* resistance mechanism (11, 14, 16, 27–31).

PDC-1 from *P. aeruginosa* contains a catalytic serine at structural alignment-based numbering of class C β -lactamases (SANC) position 64 (13) in the active site, which forms a covalent adduct with β -lactams and β -lactamase inhibitors (32). Additional key active site elements include the Ω -loop, helix 10 of the R2 region, and the Y150-S151-N152 motif in proximity to the ligand-binding site (11, 16). The Ω -loop and R2 region, in particular, are sites where clinically relevant amino acid substitutions conferring cephalosporin resistance frequently occur (15, 33). Barnes et al., previously characterized the mechanism and effects of the PDC-3 E219K substitution (referred to as PDC-3 E221K by direct sequence numbering). It was noted that the substitution enabled an alternative conformation of the Y221 residue, flipping it into an alternative plane and enabling a concomitant opening of a hidden pocket, allowing for a more catalytically favorable positioning of TOL in the active site (11). As a result of this intriguing finding, we were compelled to examine the mechanism of increased CAZ and TOL resistance in the observed clinical Y221H variant (found in PDC-85) in greater detail.

As previously reported (11), the PDC-3 E219K substitution increases resistance of isogenic *E. coli* DH10B cells expressing this PDC to TOL and CAZ, demonstrating MICs of 64 μ g/ml for CAZ and TOL, 4 μ g/ml for cefotaxime (CTX), 0.25 μ g/ml for FEP, 256 μ g/ml for ampicillin (AMP), 16 μ g/ml for PIP, 0.5 μ g/ml for IMI, and 8 μ g/ml for aztreonam (ATM) (11). In contrast,

the effect of the Y221H substitution is more subtle; the tyrosine to histidine substitution increases TOL and CAZ MICs from 0.5 and 2.0 $\mu\text{g/ml}$ respectively for PDC-3 to 8 and 16 $\mu\text{g/ml}$ for PDC-3 Y221H (11). ATM, a monobactam that shares a similar sidechain with CAZ (**Figure 1B**), demonstrated an increased MIC value from 1 to 4 $\mu\text{g/ml}$, reaching the upper limit of susceptibility (11, 34).

Consistent with the notion that β -lactamase inhibitors preserve β -lactam activity, the diazabicyclooctane (DBO) inhibitor avibactam (AVI; **Figure 1C**) restores susceptibility of CAZ (reducing the MIC from 16 to 0.5 $\mu\text{g/ml}$) and the β -lactam containing inhibitor tazobactam (TAZO; **Figure 1C**) restores susceptibility of TOL (reducing the MIC from 8 to 1 $\mu\text{l/ml}$) in the Y221H variant (11). Additionally, the BATSI LP06 reduces both CAZ and TOL MICs to 0.5 $\mu\text{g/ml}$ and S02030 reduces them to 2 and 0.5 $\mu\text{g/ml}$, respectively (11), demonstrating roughly equal effectiveness compared to two of the most crucial β -lactamase inhibitors currently used in the treatment of MDR *P. aeruginosa* infections.

We hypothesized that a similar repositioning of residue 221 comparable to that occurring in the E219K variant is responsible for this phenotype. The tyrosine to histidine substitution in Y221H occurs in the C-terminal portion of the Ω -loop, a structurally important and mobile motif involved in binding, acylation, and deacylation of cephalosporins. Our biochemical and crystallographic studies herein probed the mechanism by which PDC-3 and PDC-3 Y221H interact with CAZ and cephalothin by studying boronic acid transition state inhibitor (BATSI) analogs that mimic their deacylation transition states (LP06 and S02030, respectively; **Figure 1c**). In addition to the structural insights, we demonstrate that these BATSIs inhibit PDC-3, PDC-3 E219K, and PDC-3 Y221H with nanomolar affinity. Our studies elucidate the resistance-related structure-

function relationships in PDC-3 and PDC-3 Y221H. Furthermore, our insights into the molecular interactions of LP06 and S02030 inform ongoing β -lactamase inhibitor development efforts.

Results and Discussion

Y221H is a gain-of-function substitution that enhances catalytic activity

Using homogeneous preparations of purified enzymes and spectrophotometric methods, we determined steady-state kinetic constants for PDC-3, PDC-3 E219K (a well-characterized CAZ and TOL hydrolyzing single amino acid substitution included as a control and comparator), and PDC-3 Y221H. We employed NCF as an indicator substrate to readily assess catalytic activity. Our analysis showed that NCF K_{MS} differ only minimally between PDC-3 and the E219K and Y221H variants (28.7 μM vs 16.7 μM vs 26.2 μM), but k_{cat} values are significantly different (894.6 s^{-1} vs 76.0 s^{-1} vs 375.4 s^{-1}) (**Table 1**), with E219K turning over nearly 12-fold slower and Y221H nearly 2.5-fold slower than PDC-3 – consistent with previously observed data for E219K and other PDC variants that increase CAZ and TOL hydrolysis while decreasing the hydrolysis of other substrates (35) – suggesting that differences in NCF hydrolysis primarily result from a k_{cat} or k_3 driven process. Relative binding energy, $\Delta\Delta G_b$, of NCF to PDC-3 compared to E219K is $-4.7 \pm 0.2 \text{ kJ K}^{-1} \text{ mol}^{-1}$ and PDC-3 compared to Y221H is $-1.9 \pm 0.1 \text{ kJ K}^{-1} \text{ mol}^{-1}$. Given that ΔG_b is an algebraically negative component of the activation energy of the transition state (ΔG_T^\ddagger), a negative value of $\Delta\Delta G_b$ corresponds to an increase in ΔG_b and thus ΔG_T^\ddagger (36). This suggests that the binding of NCF to both E219K and Y221H is energetically less favorable than to PDC-3 and that the binding to E219K is energetically less favorable than to Y221H.

PDC-3 demonstrates a slow rate of hydrolysis with CAZ and TOL, hindering the use of conventional spectrophotometric methods. As a consequence of this, we employed a competition

assay (treating CAZ as a competitive “inhibitor” of NCF hydrolysis) yielding a K_I of 38.9 ± 1.3 μM , which should closely approximate the K_M (37, 38).

The E219K and Y221H variants both possess higher CAZ K_M values than PDC-3 (538.1 ± 80.0 μM and 756.5 ± 23.0 μM , respectively, compared to 38.9 ± 1.3 μM) but E219K and Y221H have measurable turnover (k_{cat} values of 5.9 ± 0.3 and 2.3 ± 0.2 s^{-1} , respectively) whereas PDC-3 does not. The combination of these measurements suggests the overall increase in hydrolysis results from a k_{cat} or k_3 driven process. Comparing catalytic efficiencies between E219K and Y221H (0.011 and 0.0031 $\mu\text{M}^{-1} \text{s}^{-1}$, respectively), we find that PDC-3 E219K is approximately 3.5-fold more efficient, consistent with the increased hydrolysis rates and MICs and corresponding to a $\Delta\Delta G_b$ of -3.1 ± 0.1 $\text{kJ K}^{-1} \text{mol}^{-1}$ for PDC-3 Y221H compared to PDC-3 E219K, suggesting binding of CAZ to Y221H is energetically less favorable than binding to E219K.

For TOL, both the E219K and Y221H variants have nearly identical K_M values (407.3 ± 24.7 and 411.3 ± 29.5 μM , respectively) which are within a single-fold difference of their corresponding CAZ values. The E219K variant has slightly over twice the turnover rate of Y221H (5.6 s^{-1} compared to 2.6 s^{-1}) leading to approximately two-and a quarter-fold greater catalytic efficiency ($\Delta\Delta G_b = -2.0 \pm 0.1$ $\text{kJ K}^{-1} \text{mol}^{-1}$ for Y221H compared to E219K), again suggesting the changes observed in hydrolysis curves and MICs are primarily k_{cat} or k_3 driven and binding to Y221H is energetically less favorable than binding to E219K.

Interestingly, when comparing CAZ and TOL hydrolysis rates, TOL is a preferred substrate, with higher catalytic efficiency (approximately 1.3 times higher in PDC-3 E219K and 2.0 times higher in PDC-3 Y221H) and positive $\Delta\Delta G_b$ (0.5 ± 0.2 $\text{kJ K}^{-1} \text{mol}^{-1}$ and 1.7 ± 0.1 $\text{kJ K}^{-1} \text{mol}^{-1}$ for TOL compared to CAZ in PDC-3 E219K and PDC-3 Y221H, respectively) corresponding to increased binding energy and thus a lower activation energy.

While neither of the variants is particularly efficient at hydrolyzing CAZ or TOL – catalytic efficiency (k_{cat}/K_M) ratios are approximately 418-fold and 4612-fold lower for CAZ and 328-fold and 2306-fold lower for TOL compared to NCF for E219K and Y221H, respectively – both variants confer higher MICs, particularly when combined with other resistance mechanisms as is the case in clinical *P. aeruginosa* strains. This is a common phenomenon with expanded-spectrum AmpC (ESAC) Ω -loop variants, as MICs are often elevated only within a narrow range around the resistance threshold (16, 23, 39, 40).

Mass spectrometry captures CAZ and TOL acyl-enzyme complexes with PDC-3, PDC-3 E219K, and PDC-3 Y221H

To provide additional mechanistic insight, we utilized timed electrospray ionization mass spectrometry (ESI-MS) experiments to determine the intermediates of the interaction between substrates (CAZ and TOL) and β -lactamases (PDC-3, PDC-3 E219K, and PDC-3 Y221H). Two major species were noted for all enzymes, corresponding to the presence or absence of the N-terminal methionine residue (+131 Da; **Table 2**) introduced by the insertion of an NdeI restriction site immediately upstream of the 5' end of the coding sequence for the mature protein, as previously reported (11, 14).

Testing a 1:50 molar ratio of β -lactamase to substrate, complexes were observed at 15 (**Figure 2**) and 30 (**Figure S1**) seconds between CAZ and TOL with PDC-3, PDC-3 E219K, and PDC-3 Y221H, demonstrating acylation with both antibiotics by all three enzymes. As expected, relative abundances of the acyl-enzyme complexes were lower than the apo enzymes due to the relatively high K_M values of CAZ and TOL. Importantly, using a 50-fold higher concentration of antibiotic than in previous reports enabled the capture of a PDC-3/TOL complex which was not

previously observed (likely due to the extremely high K_M , 1.3 mM, and steric hinderance complicating entry into the active site as previously reported) (11). This complex appearing at a similar level to the complexes of TOL with PDC-3 E219K and PDC-3 Y221H suggests that formation of the acyl enzyme complex is not a rate limiting step under the conditions tested and is consistent with the kinetic results supporting turnover-driven rather than K_M -driven rate enhancement.

Time course data (**Figure S2**) reveals that the acyl-enzyme complex is long-lived between CAZ and PDC-3 but diminishes in proportion over time with E219K and Y221H, consistent with repeated cycles of hydrolysis reducing substrate concentration in the reaction and occupancy of the active sites as assessed by relative abundance of the acyl-enzyme complex. A similar pattern is observed with TOL (**Figure S3**), supporting the kinetic interpretation of increased hydrolysis by PDC-3 E219K and PDC-3 Y221H compared to PDC-3.

Assessing the impact of the Y221H substitution on thermal stability using CD and DSF

The thermal stability of PDC-3, E219K, and Y221H were determined using circular dichroism (CD) and equilibrium unfolding curves (**Figure 3A**). These experiments revealed that the Y221H variant is less stable compared to PDC-3, with T_M decreasing 4°C (from 51.1°C in PDC-3 to 46.9°C in the Y221H variant) and corresponding to a $\Delta\Delta G_u$ of $-6.21 \text{ kJ mol}^{-1} \text{ K}^{-1}$, but more stable compared to E219K ($T_M = 45.3 \text{ }^\circ\text{C}$; $\Delta\Delta G_u = -8.48 \text{ kJ mol}^{-1} \text{ K}^{-1}$). These decreases are suggestive of increased flexibility within the β -lactamase, most likely in the Ω -loop, leading to either increased access or more favorable positioning of substrate in the active site. Decreases in thermal stability are commonly reported in connection with substrate profile expansion in serine β -lactamases and are often associated with increased flexibility (41–45).

In addition to CD, we also used DSF to measure, the T_m for PDC-3 and Y221H in both the absence and presence of 150 μ M of LP06 and S02030. As ligands LP06 and S02030 were dissolved in DMSO (which has an intrinsic CD signal), the equivalent amount (1.5%) of DMSO was added to the control reactions. The measured T_m of PDC-3 in the absence of ligands was 47.2 ± 0 °C and in the presence of LP06 and S02030 was 58.4 ± 0 °C and 58.6 ± 0 °C, respectively (**Figure 3B**). The T_m of apo PDC-3 Y221H was 42.6 ± 0 , a decrease by 4.6 °C compared to PDC-3. When complexed with BATSI, the T_m for the Y221H variant increased to 52.4 ± 0 °C and 50.1 ± 0.1 °C in the presence of LP06 and S02030, respectively (**Figure 3B**). Similar LP06 and S02030 induced stabilization of PDC-3 was observed previously using circular dichroism (11).

Both modalities of evaluating thermal denaturation indicate that the Y221H variant has a lower T_m , suggesting it is a less stable β -lactamase and that both BATSI compounds stabilize PDC3 and Y221H.

Effects of Inhibitors on PDC-3 and Y221H

Because of their chemical similarities to β -lactam antibiotics, BATSI are often used as probes to understand the mechanism of β -lactamase inhibition. Both BATSI compounds – LP06 and S02030 – are potent inhibitors of PDC-3, PDC-3 E219K, and PDC-3 Y221H, possessing nanomolar IC_{50} values (**Table 4**). Interestingly, these inhibitors have lower IC_{50} values than AVI against PDC-3. The BATSI have somewhat higher IC_{50} values against E219K and Y221H, suggesting they are slightly less effective inhibitors of the variants, but still fall in the nanomolar range shared with AVI and TAZO and indicative of effective inhibitors.

Consistent with our previous study (11), both LP06 and S02030 stabilize PDC upon binding, raising T_m (**Table 5**) at a 1:10 ratio of enzyme to inhibitor by between 2.1°C and 5.5°C,

with PDC-3 stabilized the most and E219K the least. Changes in the free energy of unfolding ($\Delta\Delta G_u$) help to quantify the thermodynamic effects of inhibitor binding and reveal the energetic changes are generally smaller in magnitude than those corresponding to the differences between PDC-3 and either the E219K or Y221H variant. Interestingly, both BATSIs exhibit greater stabilization than either AVI or TAZO (TAZO used at a 1:1 ratio due to the presence of a high intrinsic CD signal), with AVI slightly destabilizing two of the three enzymes.

The decrease in thermal stability upon AVI binding does not appear to have been reported previously, but similar results have been observed with at least one other DBO (46). As it is not unique to PDC-3 Y221H, further investigation of this phenomenon is outside the scope of this study but poses an interesting question for future research efforts.

Crystal structures of apo PDC-3 and apo Y221H PDC-3

The crystal structures of PDC-3 and PDC-3 Y221H are very similar as their superimposition yields a r.m.s.d. of 0.20 Å for 349 C α atoms (**Figure 4**). Note that in both the active site of apo-PDC-3 and apo-Y221H PDC-3, an isopropyl alcohol (IPA) molecule present in the crystallization solution is observed in the electron density. In the PDC-3 structure, the oxygen atom of IPA makes three hydrogen bonds (with O γ atom and main chain N atom of S64, and with the main chain nitrogen atom of S318). In the PDC-3 Y221H structure, IPA makes similar hydrogen bonds as in the PDC-3 structure (**Figure 4**).

The major difference between the PDC-3 and PDC-3 Y221H structures is that part of the Ω -loop is disordered in the PDC-3 Y221H structure; residues 205-212 are not observed in the electron density and are thus not modeled in the PDC-3 Y221H structure (**Figure 4B-4C**). PDC-3

residue Y221 makes hydrophobic interactions with the hydrophobic atoms of Ω -loop residue D217. In addition, Y221 makes two water-mediated interactions with backbone oxygens of P213 and P215. The side chain of D217 makes Ω -loop stabilizing interactions via hydrogen bonds with backbone nitrogens of G214 and A218 as well as with the K126 side chain (**Figure 4**). In the PDC-3 Y221H structure, the side chain of H221 is rotated 140°, now pointing towards S64. As a consequence, the hydrophobic interactions of Y221 with D217 are absent, allowing residue D217 to adopt two conformations in the PDC-3 Y221H with conformation #2 occupying the space that Y221 occupies in PDC-3. An additional difference involves the reorientation of the backbone oxygen of N320 in the PDC-3 Y221H structure (**Figure 4C**). The adjacent nitrogen of this peptide backbone moiety in PDC-3 is making a water-mediated interaction with the Ω -loop, an interaction no longer possible in the PDC-3 Y221H structure. The loss of the water-mediated Ω -loop interactions of Y221 and that D217 occupies two conformations with its second conformation having lost the Ω -loop stabilizing interactions is the likely cause of the observed disorder of Ω -loop residues 205-212. We propose the Ω -loop destabilization observed in the PDC-3 Y221H structure likely is at the basis of the 4.6 °C lower T_m (**Figure 3B**).

The variability of the residue 221 side chain orientation and concomitant Ω -loop disorder in the PDC-3 Y221H variant could explain why this variant has increased resistance to CAZ (11). Shifting of Y221 in a tripeptide insertion resistance variant of GC1 were found to allow CAZ to adopt a catalytically competent conformation that did not destabilize the tetrahedral deacylation transition state, thus enabling hydrolysis (47–49). Residue Y221 is near where CAZ's aminothiazole ring binds in the acylation complex state and forms quadrupole interactions in the related ADC-7 β -lactamase (and likely also in the Michaelis-Menten complex) (50). Side chain orientation variability at position 221 and the Ω -loop disorder could allow CAZ to be better

accommodated during certain catalytic steps. Molecular dynamics simulations suggested that side chain variability at position 221 could also play a role in the resistance phenotype of PDC-3 E219K (11). The related CMY-2 β -lactamase can also harbor the Y221H resistance mutation (CMY-136), yielding increased resistance to ticarcillin, cefuroxime, cefotaxime, and TOL/TAZO (but not CAZ) (51). The structure of CMY-136 showed a similar H221 reorientation concomitant with increased disorder/flexibility in the Ω -loop (51). That the same Y221H substitution gives rise to resistance to different β -lactams suggests that additional active site amino acid differences contribute to these resistance phenotypes.

The structure of PDC-3 is very similar to that of PDC-1 (PDB id accession code 4GZB) (32). The root-mean-square-deviation (r.m.s.d.) of superimposing these two structures is 0.38 Å for 359 C α atoms. PDC-1 and PDC-3 differ by one amino acid (i.e., T79A change in PDC-3) and have very similar MICs (11, 16), although an earlier publication reported kinetic and microbiological differences (12). Residue 79 is partially solvent-exposed and is at the C-terminus of helix H2; the N-terminus of this helix contains the catalytic S64. Although the phenotypic impact of the T79A variation is uncertain, it is possible that changes in the C-terminal end of helix H2 could have an impact on the S64 movements needed for catalysis.

Complexes of PDC-3 and PDC-3 Y221H with LP06

Soaking in LP06 into PDC-3 and PDC-3 Y221H crystals revealed the presence of this inhibitor bound in the active site (**Figures 5 and 6**). Inhibitor density was continuous with the O γ atom of the catalytic S64, indicating a covalent bond between the β -lactamase and LP06. As expected for BATSI, the electron density map is consistent with a tetrahedral geometry about the boron atom of LP06 in both of the complex structures. The LP06 complexes of PDC-3 and PDC-3 H221Y are

virtually identical: their superimposition yields a r.m.s.d. of 0.14 Å for 360 C α atoms. The active site ligand interactions are also nearly identical. One of the boronic acid hydroxyls is bound in the oxyanion hole and makes two hydrogen bonds with main chain N-atoms of S64 and S318 and a third hydrogen bond with the backbone oxygen of S318 (**Figures 5 and 6**). The second boron hydroxyl of the inhibitor hydrogen bonds with the side chain of Y150. LP06 contains the R1 side chain of the CAZ, and the interactions this group makes with the enzyme are virtually identical in both LP06 complexes. The R1 amide oxygen atom hydrogen bonds with Gln120 and Asn152. The aminothiazole amino group makes both a direct and water-mediated hydrogen bond with N320 (**Figures 5 and 6**). Electron density for the dimethyl-carboxyl group of the inhibitor is relatively weak; this moiety is not making direct hydrogen bonds with the protein. The dimethyl groups of the dimethylcarboxyl moiety make hydrophobic interactions with A292, L293, and L119 (**Figures 5 and 6**). The dimethylcarboxyl moiety of LP06, when bound to the related ADC-7, is less ordered (50). However, LP06 in this latter structure contains an (unexpected) covalently attached phosphate moiety instead of a boron hydroxyl group (50) thus dampening the impact of structural comparisons with the ADC-7 LP06 complex.

LP06 binding to both PDC-3 and PDC-3 Y221H yields similar protein conformations regarding both the orientation of residue 221, the main chain of N320, and the conformation and order of the Ω -loop (**Figures 5 and 6**). This indicates that LP06 induced a PDC-3 protein conformation for PDC-3 Y221H (r.m.s.d. for apo and LP06 bound PDC-3 Y221H is 0.24 Å for 349 C α atoms). LP06 also induces the side chain of D217 in the single PDC-3 conformation, thus stabilizing the Ω -loop interactions. These LP06-induced structural observations agree with the observed significantly increased T_m values of PDC-3 and PDC-3 Y221H when bound to LP06

(Figure 3B). The significant number of interactions of LP06 in the PDC-3 active site aid in explaining its potent affinity ($IC_{50} = 4.6$ nM).

LP06 also inhibits FOX-4, but its 110 nM IC_{50} is 24-fold higher than for PDC-3 (52). Superimposition of the LP06 bound complexes of PDC-3 and FOX-4 indicate that the aminothiazole ring moieties are in different positions (**Figure 7**), and the dimethyl carboxyl moiety was too disordered to be modeled in the FOX-4 complex (52). The LP06 aminothiazole moiety, when bound to FOX-4, is near Y221, whereas this moiety is more distant from Y221 in the PDC-3 complex. This is likely a consequence of the presence of N320 in PDC-3 (it is G320 in FOX-4) as this side chain hydrogen bonds with the aminothiazole ring (**Figures 6 and 7**). Amino acid differences in FOX-4 near where the dimethyl moiety of LP06 binds in PDC-3 (i.e., A292S and L293F) could also, in part, contribute to why LP06 inhibits FOX-4 more weakly when compared to PDC-3 (**Figure 7**).

Complexes of PDC-3 and PDC-3 Y221H with S02030

Soaking inhibitor S02030 into crystals of PDC-3 and PDC-3 Y221H yielded active site density for the covalent inhibitor (**Figures 8 and 9**). Like LP06, the electron density map of S02030 also shows a tetrahedral geometry about the boron atom in both of the complex structures. The boronic acid hydroxyl moieties make similar interactions as in the LP06 bound structures, except that the hydroxyl in the oxyanion hole is not as deeply located in this oxyanion hole. This minor shift causes the hydroxyl's hydrogen bond with the backbone oxygen of S318, present in the LP06 complexes, to be absent. This conformational difference is likely due to the presence of the adjacent R2 group of S02030; LP06 does not have an R2 group (**Figure 1C**). The amine group of S02030 makes hydrogen bonds across the width of the active site: with the side chain of N152 and

with the backbone oxygen of S318 (**Figures 8 and 9**). The amine group is also making van der Waals interactions with the side chain of Y221/H221 in the structures. The S02030 R2 group, when bound to PDC-3 is observed in two conformations, whereas it is observed in a single conformation when complexed to PDC-3 Y221H (**Figures 8 and 9**). The carboxyl moiety of the R2 group makes a hydrogen bond with N343. The R1 thiophene ring of S02030 is observed in two conformations in the PDC-3 Y221H complex and is in a single conformation when bound to PDC-3. The thiophene ring conformations make van der Waals interactions with N320.

Regarding the protein conformation, the S02030 PDC-3 and PDC-3 Y221H complexes are very similar; their superimposition yields a r.m.s.d. of 0.31 Å for 359 C α atoms. Superimposition of the PDC-3 LP06 and PDC-3 S02030 complexes yield a r.m.s.d. of 0.11 Å for 359 C α atoms indicating again a very similar protein conformation. Residue 221 is in each case in a similar position as in the LP06 complexes pointing away from S64. Furthermore, the Ω -loop is in an ordered PDC-3 conformation in both S02030 complexes. The S02030 conformation is, however, more variable: its R1 and R2 positions displaying alternate conformations and even the R1 group in the PDC-3 Y221H complex is in a different orientation as in the PDC-3 complex (**Figures 8 and 9**). Compared to the PDC-3 S02030 complexes, different R1 and R2 conformations are also observed for S02030 bound to related class C β -lactamases ADC-7 (53) and MOX-1 (54).

Compared to LP06, S02030 makes fewer hydrogen bonds and van der Waals interactions in the PDC-3 and PDC-3 Y221H active sites. This observation is likely the basis for the slightly lower 8.5 nM affinity of S02030 for PDC-3 compared to the 4.6 nM affinity of LP06.

Molecular docking studies

In silico docking studies were performed to gain insights the binding modes of the ligands CAZ and TOL bound to PDC-3 and Y221H. **Figures S4, S5, and S6** show the results of covalent docking with the ligands forming an acyl intermediate. **Table S2** lists the docking scores obtained from these covalent docking calculations. CAZ and TOL binding to PDC-3 yielded better docking scores (-6.137 and -7.834, respectively) in comparison to those for PDC-3 Y221H (-5.653 and -6.306, respectively) suggesting that the latter variant has weaker affinity for these ligands. The docking results for PDC-3 indicate that CAZ makes a covalent bond with S64 and 11 hydrogen bonds with Y150, N152, N320, N343, S318, N346, T316. TOL also is predicted to make a covalent bond with S64 and 12 hydrogen bonds with Y150, T316, S318, N320, N343, N346. Overall, the docking poses for CAZ and TOL bound to PDC-3 indicate that the active site of PDC-3 can accommodate both β -lactams with the commonly observed oxyanion interactions for the carbonyl oxygen (which is also observed for one of the boronate hydroxyl moieties such as for BATSILP06 binding to PDC-3) (**Figures 5C and 5D**). Regarding their docked binding mode to PDC-3 Y221H, the CAZ and TOL orientations are about 180° rotated in the active site compared with when bound to PDC-3 and their carbonyl oxygens are not positioned in the oxyanion hole (**Figures S4 and S5**). These different substrate orientations are likely due to the reorientation of H221 pointing inward (**Figure 4B**) compared to the outward orientation of Y221 in PDC-3. Despite the difference in orientation, CAZ is predicted to have a covalent bond with S64 and make 7 hydrogen bonds with K67, Y150, H221, E272, T289, T316, N346, whereas TOL is predicted to make 6 hydrogen bonds with Y150, N152, H221, E272, T316, N320. These docking conformational differences and score differences could explain why CAZ has a higher K_m for PDC-3 Y221H compared to PDC-3. An alternative explanation is that CAZ binding might only occur in PDC-3 Y221H with the histidine side chain in the outward position as was observed for LP06 binding. This outward conformation

of H221 likely only occurs in a small population in PDC-3 Y221H with the major population being the inward conformation that is crystallographically observed. Thus, CAZ perhaps only being able to bind to a conformation of PDC-3 Y221H that only a minority of PDC-3 Y221H proteins adopt could thus also explain the higher K_m compared to PDC-3. Note we do realize that determining binding affinity via docking calculations is not yet very accurate (55) but comparing the docking scores of ligands CAZ and TOL (**Table S2**) and their different orientations could yield insights into their relative binding affinities to PDC-3 and Y221H PDC-3 enzymes.

The Y221H substitution also increases hydrolysis of CAZ and TOL that is very slow or not measurable for PDC-3. Based on our docking results, there are possibly three explanations for the observed increase in hydrolysis by PDC-3 Y221H. The first is that the thiazole ring of CAZ and similar thiadiazole ring in TOL could act as a base to activate the water-mediated deacylation reaction for these ligands in a substrate-assisted manner as was hypothesized for the D179Y KPC-2 variant (56). These rings are in closer proximity to the acyl-bond in the docked PDC-3 Y221H mutant than in the PDC-3 structures. A second explanation could involve the imidazole ring of H221 in the inward orientation being in the vicinity of the acyl bond and could act as a base to withdraw a proton from a nearby water molecule to facilitate deacylation of CAZ and TOL. Histidines are known to be able to be a proton donor or acceptor (57). H221 residue is within 3.5 Å distance of the catalytic S64 and could be important for hydrolyzing CAZ and TOL. Thirdly, the Y221H caused disorder of the nearby Ω -loop which enlarges the active site which could allow CAZ and TOL to acylate and deacylate more productively despite the weaker binding affinities of CAZ and TOL in PDC-3 Y221H. The Ω -loop is closer to the docking binding modes of CAZ and TOL in the PDC-3 than in the PDC-3 Y221H docked structures. In particular, the thiazole and thiadiazole rings of the β -lactams are near to the Ω -loop in the PDC-3 Y221H structures. This third

explanation would have CAZ and TOL binding to PDC-3 Y221H in the binding mode as when docked to PDC-3 possibly allowed by an outward orientation of H221. Of the three explanations, the latter maintains the β -lactam carbonyl oxygens in the oxyanion hole which is needed to stabilize the transition state intermediate and suggests that Y150 provides the electron needed for base-assisted catalysis.

WT-MetaDynamics simulations and structural models reveal alternate conformations of Y221H

Enhanced sampling well-tempered metadynamics simulations were run to sample the conformational landscape of the PDC-3 and the Y221H variant. The simulations were stopped at 3 μ s after the convergence was achieved for both systems (**Figures S7 and S8**). The Free energy surface (FES) plots were calculated for both PDC-3 and Y221H variant structures as a function of the ϕ and ψ dihedral angles of residue 221. Distinct basins were identified highlighting regions of lowest energy states (**Figure 10**), wherein each basin corresponds to an ensemble of conformations of the protein. The FES plots in both, PDC-3 and the Y221H variant are quite similar. There are two free energy basins (labelled A and B), containing one dominant cluster. The exemplar structure from each basin was extracted and further analyzed for the differences in the dynamics of the tyrosyl side chain in PDC-3 and the imidazole ring of the H221 variant. The residues in the active site show few differences in basin A. The tyrosyl side chain in the PDC-3 Y221 orients towards the Ω loop (**Figure 10**). The side chains of K67, Y150 and the catalytic S64 are oriented as in the crystal structure. In case of the Y221H variant, the imidazole side chain points inwards into the active site. This is the conformation observed in the crystal structure of the apo state of the Y221H variant. In basin B, in PDC-3, the side chain of Y221 rotates, but still points towards the Ω loop. The side chain orientations of K67, Y150 and S64 are similar to those observed in the crystal

structure. Comparing FES maps between PDC-3 and the Y221H variant, basin B in the Y221H variant is shifted, indicating a different free energy minimum for the structure. A detailed structural analysis reveals a similar conformation of the imidazole side chain as observed in the crystal structure, however, the side chain of Y150 is rotated away from the active site.

Conclusions

Based upon previous investigations, we continue to elucidate the roles of amino acid substitutions in the emergence of TOL and CAZ resistance in PDC. Herein, we demonstrate that the Y221H substitution in PDC-3 substantially increases hydrolysis of both CAZ and TOL and it does so primarily by a k_{cat} (turnover) driven mechanism. Structural analyses by both MetaDynamics simulations and X-ray crystallography support the notion that the sidechain of the H221 residue favors a conformation in a different plane than Y221, opening a hidden pocket that likely allows the substrates to assume different conformations in the active site. Molecular docking revealed three possible factors which may contribute to increased turnover: 1) the substrate serving as a base to activate the deacylation water; 2) an alternative general base to activate the deacylation water, or; 3) the ability to take on more catalytically favorable conformations as a result of decreased order in the Ω -loop, resulting in enlargement of the active site. While the substitution decreases hydrolysis of smaller substrates (NCF), the impact on inhibitors is minimal and the BATSIs LP06 and S02030 are effective inhibitors of both PDC-3 and the Y221H variant, suggesting that ongoing development of newer iterations of these BATSIs should continue to provide a promising pathway to inhibiting CAZ and TOL resistant PDC variants caused by Ω -loop alterations.

As previously demonstrated in class A β -lactamases (58, 59), PDC (11), and other class C β -lactamases (50, 53, 54), the BATSIs LP06 and S02030 are potent inhibitors of PDC-3, E219K, and Y221H with nanomolar IC_{50} values. They form large numbers of interactions with the enzymes and stabilize the enzyme-inhibitor complex in the process. Ongoing studies with newer generations of BATSIs continue to build on these results as we optimize for both coverage and potency.

Finally, based on the data presented herein, previous work on PDC (11, 14, 29), and literature reports of Ω -loop substitutions and insertions occurring in both PDC (60) and other class C β -lactamases (48, 51), we hypothesize that the Y221 residue plays a crucial and hereto underappreciated role in the development of resistance to CAZ and TOL. By either directly or indirectly repositioning the sidechain of the 221 residue, substitutions occurring at several positions in the C-terminal portion of the Ω -loop increase turnover of these important anti-*Pseudomonas* cephalosporins, likely through the opening of an otherwise hidden pocket in the active site allowing repositioning of the substrate into a more catalytically favorable orientation. We also propose that the Y221 residue represents an important focus for the development of inhibitors or antibiotics looking to overcome or avoid the development of these and similar resistance mechanisms. We close with the observation that despite best efforts in strategic drug design, natural protein engineering in the Ω -loop of class C β -lactamases uncovers novel catalytic properties contributing to antimicrobial resistance.

Materials and Methods

Key Reagents

CAZ was purchased from MilliporeSigma (Saint Louis, MO, USA). Merck & Co., Inc. (Kenilworth, NJ, USA) provided TOL as part of a research agreement. AVI was purchased from Advanced ChemBlocks (Hayward, CA, USA). Nitrocefin (NCF) was purchased from ThermoFisher Scientific (Waltham, MA, USA). TAZO was purchased from Chem-Impex International (Wood Dale, IL, USA). BL21-CodonPlus (DE3)-RP Competent Cells were purchased from Agilent Technologies (Santa Clara, California, USA). The BATSI compounds LP06 (61) and S02030 (58) were synthesized as previously described.

Protein Expression and Purification

The β -lactamases were expressed and purified with modifications to previously described protocols (11). Plasmids were prepared as previously described (11). Briefly, plasmids containing expression constructs (pET24a(+)-SK(-)-*bla*_{PDC-3}, pET24a(+)-*bla*_{PDC-3 E219K}, and pET24a(+)-*bla*_{PDC-3 Y221H}) were transformed into BL21-CodonPlus (DE3)-RP cells, grown on lysogeny broth (LB) agar plates containing kanamycin (KAN) and chloramphenicol (CHL) as selective agents, and stored at 4°C for up to one month for subsequent use. Overnight cultures in LB with KAN and CHL were started from five isolated colonies and used to inoculate 3L of Super Optimal Broth (SOB). Large-scale cultures were shaken at 37°C for approximately three hours, grown to an OD₆₀₀ of 0.8 to 1.0, induced with 0.5 mM Isopropyl β -D-1-thiogalactopyranoside (IPTG), cooled to 18°C, and shaken overnight. After 18 to 20 hours, cells were pelleted and frozen at -20° for later use.

Cell pellets were thawed and resuspended in a lysis buffer consisting of 20 mM Tris pH 7.5, 25 mM sucrose, 40 µg/ml lysozyme, 1mM MgSO₄, 100 mM NaCl, and 250 U Benzonase nuclease (Millipore Sigma). Cells were lysed, pelleted at 18,500 x g for 1 hour at 4°C, and supernatants transferred to dialysis tubing for consecutive 3 hour and 1 x overnight dialyses against 2 L of Tris-sucrose buffer (20 mM Tris, pH 7.5, and 25 mM sucrose). Dialyzed supernatant was centrifuged at 18,500 x g for 1 hour and loaded onto a prepared HiTrap SP HP cation exchange column (Cytiva Life Sciences, Marlborough, MA, USA). The column was washed with ten column volumes of Tris-sucrose buffer and eluted with an increasing gradient of 500 mM NaCl in Tris-sucrose buffer to facilitate cation exchange. Fractions were collected when UV absorbance was greater than 25 mAu and purity assessed by SDS-PAGE. Pooled fractions were buffer exchanged into PBS, concentrated using Amicon Ultra Centrifugal Filtration Units (Millipore Sigma), and run on a HiLoad 16/600 Superdex 75 pg size exclusion column (Cytiva Life Sciences) for final purification. Purity was assessed by SDS-PAGE, fractions pooled, and concentration determined by A₂₈₀ readings. Enzymes were sterile filtered and stored at 4°C until needed.

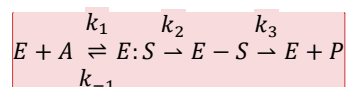
Steady-state kinetic analysis

β-Lactamase kinetic measurements were conducted using Agilent 8453 or 8454 UV-visible Spectroscopy Systems (Agilent Technologies, Santa Clara, CA, USA) and Suprasil Quartz Absorption cuvettes (Hellma Analytics, Müllheim, Germany) with either a 1.0 cm or 0.1 cm path length as appropriate. Activity buffer was 1x PBS, pH 7.4 with 200 µg/ml bovine serum albumin (BSA) to enhance enzyme stability. With NCF (a readily hydrolyzed chromogenic cephalosporin used as an indicator substrate), reads were taken every 0.5 seconds for 10 to 20 seconds (corresponding to the linear portion of the progress curve). With CAZ and TOL, reads were taken

every 10 seconds (to minimize the extent background UV-mediated hydrolysis) for the duration of the linear portion of the progress curve, up to a maximum of 300 seconds. Data was collected and initial rates determined using UV-Visible ChemStation software version B.05.02 (Agilent Technologies). Data processing and analysis was performed using Origin Version 2022 (OriginLab, Northampton, MA) and Excel (Microsoft Corporation, Redmond, WA, USA).

Substrates were measured at the following wavelengths (λ) and extinction coefficients ($\Delta\epsilon$): NCF $\Delta\epsilon = 17,400 \text{ M}^{-1} \text{ cm}^{-1}$ at $\lambda = 482 \text{ nm}$ (38); CAZ $\Delta\epsilon = -7,600 \text{ M}^{-1} \text{ cm}^{-1}$ at $\lambda = 256 \text{ nm}$ (62); and TOL $\Delta\epsilon = -9900 \text{ M}^{-1} \text{ cm}^{-1}$ at $\lambda = 270 \text{ nm}$. The $\Delta\epsilon$ for TOL was determined by monitoring the complete hydrolysis of $100 \mu\text{M}$ TOL using 100 mM NaOH and calculated using the Beer-Lambert law.

The reaction mechanism for cephalosporin hydrolysis by PDC can be represented by the following rate equation, where $K_M = \frac{k_{-1} + k_2}{k_1}$:



Commented [MAR(1): Note: the area under the k2 and k3 arrows should be empty. Word displays a dotted box because nothing is entered in the placeholder.

Equation 1

The kinetic constants K_M and V_{\max} were determined using a nonlinear least-squares regression of the data to the Henri-Michaelis-Menten equation (Equation 2) in Origin, where v is the velocity of the reaction, V_{\max} is the theoretical maximum velocity, K_M is the Michaelis constant, and $[S]$ is the substrate concentration:

$$v = \frac{V_{\max}[S]}{K_M + [S]}$$

Equation 2

Change in free energy of binding between the enzyme and the transition state ($\Delta\Delta G_b$) was calculated using the following equation (36), where R the ideal gas constant ($8.314463 \text{ J mol}^{-1} \text{ K}^{-1}$) and T the temperature in Kelvin (296.5 K) :

$$\Delta\Delta G_b = -RT \ln \left(\frac{\left(\frac{k_{cat}}{K_M} \right)_A}{\left(\frac{k_{cat}}{K_M} \right)_B} \right)$$

Equation 3

Competitive inhibition assays were used to determine IC_{50} . NCF (a reporter substrate), enzyme, and inhibitor were mixed and initial velocities determined over ten to fifteen seconds. Inhibition values were determined after a five-minute preincubation. Inverse steady-state velocities ($1/V_0$) were plotted against inhibitor concentration ([I]), forming a straight line. The y-intercept of this line was divided by the slope of the line to yield $IC_{50 \text{ obs}}$ values. Corrected IC_{50} values were determined by correcting for affinity of NCF in the active site using Equation 4:

$$IC_{50} = \frac{IC_{50 \text{ obs}}}{1 + \frac{[S]}{K_M \text{ NCF}}}$$

Equation 4

Electrospray ionization mass spectrometry (ESI-MS)

Five micrograms of PDC-3, PDC-3 E219K, or PDC-3 Y221H was incubated at the indicated molar ratio in a total volume of 20 μl in 1X PBS, pH 7.4 at room temperature for the duration of the indicated timepoints. Reactions were quenched with the addition of 10 μl acetonitrile and added to 1 ml of 0.1% formic acid in water.

Data was collected using a Waters (Milford, MA, USA) Synapt G2-Si Quadrupole time-of-flight (Q-TOF) mass spectrometer and Waters Acquity UPLC BEH C₁₈ 1.7- μ m column (2.1 by 100 mm). MassLynx V4.1 was used to deconvolute protein peaks. Mobile phase A was 0.1% formic acid in water. Mobile phase B was 0.1% formic acid in acetonitrile. Instrument settings were as previously described (11). The mass accuracy of this system is ± 5 Da.

Thermal Denaturation

Experiments were conducted by circular dichroism using a Jasco J-815 CD Spectrophotometer and Jasco CDF-426S/15 Peltier temperature control module based on previously reported protocols (11). Purified enzyme (PDC-3, PDC-3 E219K, or PDC-3 Y221H) either alone or in the presence of 50 μ M AVI, LP06, or S02030 or 5 μ M TAZO (to minimize the effect of the high intrinsic CD signal) were monitored by CD at 208 and 222 nm (corresponding to the CD maxima for α -helices) between 20° and 70°C at a heating rate of 2°C per minute. Measurements were conducted using a 0.2 cm path length Quartz cuvette (Hellma Analytics). Two-state behavior was indicated by identical curves at each of the monitored wavelengths. Raw melting curves were normalized to the fraction unfolded protein (f_U) using the equation $f_U = [F]/([F]+[U]) = (\theta_t - \theta_U)/(\theta_F - \theta_U)$ where θ_t is the ellipticity at a given temperature and θ_F and θ_U are the ellipticities of the fully folded and unfolded forms, respectively (63). Given a reversible two-state transition between the native and unfolded forms, equilibrium constants (K_{eq}) were calculated using Equation 5 (11, 64).

$$K_{eq} = \frac{f_U}{1 - f_U}$$

Equation 5

Assuming that enthalpy and entropy changes are constant with temperature ($\Delta C_p = \text{constant}$) (65), the Gibbs Free Energy ($\Delta G = \Delta H - T\Delta S = -RT\ln K_{\text{eq}}$) and van't Hoff equation (Equation 6) were used to determine the melting temperature (T_m). The ΔH and ΔS values were determined from the slope of a plot of $\ln(K_{\text{eq}})$ vs $1/T$ using Equation 6 (63). T_m values were determined at the midpoint of unfolding equilibrium ($\Delta G_u = 0$) and reported as the average of value at $\lambda = 208 \text{ nm}$ and $\lambda = 222 \text{ nm}$ (tracking the presence of α -helical secondary structure).

$$\ln K_{\text{eq}} = -\frac{\Delta H}{RT} + \frac{\Delta S}{R}$$

Equation 6

The difference in free energy of unfolding ($\Delta\Delta G_u$) was determined by the method of Becktel and Schellman (65) using the equation $\Delta\Delta G_u = \Delta T_m \Delta S_u^{\text{WT}}$. At $T = T_m$, the Gibbs Free Energy equation becomes $\Delta S_u = \frac{\Delta H_u}{T}$ and $\Delta S_u^{\text{WT}} = 1.46 \text{ kJ mol}^{-1} \text{ K}^{-1}$.

Differential Scanning Fluorimetry (DSF)

For both PDC-3 and Y221H proteins, a final concentration of $10 \mu\text{M}$ was used in 1X PBS buffer, pH 7.4. The total reaction volume for each sample was $30 \mu\text{L}$, and 10X SYPRO Orange dye was used for fluorescence measurements during the thermal denaturation from $25 \text{ }^\circ\text{C}$ to 70°C . Experiments were performed in duplicate, and the fluorescence signal was read out on a CFX96 Touch ThermoCycler (Bio-Rad).

Crystallization, data collection, and crystallographic refinement

Crystals for both PDC-3 and the Y221H variant were obtained by mixing protein and reservoir solution in 1:1 ratio using the sitting drop crystallization method. The protein was concentrated to

10 mg/mL in 10 mM HEPES pH 7.5, 150 mM NaCl and 5% glycerol. The crystallization drops contained 1.5 μ L of the protein and 1.5 μ L of the reservoir solution (100 mM Imidazole pH 7.0, 2-8% isopropyl alcohol (IPA), and 16-34% PEG 3350). Rod-like protein crystals grew after 2-3 days of incubation at 20 °C. These crystals were used for soaking the BATSI compounds. LP06 was soaked at 3 mM for 45 hours for PDC-3 and at 2 mM for 30 minutes for the Y221H variant crystals. The BATSI S02030 was soaked at 5 mM for 5 hours for PDC-3 and at 2 mM for 3 hours for Y221H variant crystals. After soaking, the crystals were frozen in liquid nitrogen for data collection. Data were collected at two different synchrotrons facilities - NSLS beamline FMX and SSRL beamlines BL12-2 and BL9-1 and processed using XDS (66) and HKL3000 (67), respectively. All the structures were solved via molecular replacement with MOLREP (68) using the AmpC β -lactamase from *P. aeruginosa* coordinates as the search model (Protein Data Bank (PDB) accession code 3S22 (69)). The structures were refined using REFMAC (70), and the model building was done using COOT (71). After the first round of refinement, the electron density for the ligands was observed in the active site pocket covalently attached to residue S64. Refinement parameters for the ligands LP06 and S02030 were generated using AceDRG (72), and the ligands were included in subsequent refinement steps. Additional ligands like isopropyl alcohol (IPA), dimethyl sulfoxide (DMSO), and imidazole (IMD) were also located in the electron density and therefore included in the final rounds of refinement. The apo forms of PDC-3 and Y221H were solved at 1.75 Å and 2.1 Å resolutions, respectively. The crystal structures of LP06 in complex with PDC-3 and Y221H mutant proteins were determined to the resolutions of 1.35 Å and 1.65 Å, respectively (**Table 5**) and for S02030 at 1.38 Å and 1.42 Å, respectively. All the structures were solved in the P2₁2₁2₁ space group with one molecule in the asymmetric unit. The quality of the models was analyzed with the PDB validation server (www.wwpdb.org). Overall, 100% of

residues were in the favored and allowed regions of the Ramachandran plots for all the complex structures (**Table 5**). Molecular figures were generated using Pymol (www.pymol.org).

Covalent docking of CAZ and TOL into PDC-3 and PDC-3 Y221H

Molecular docking of CAZ and TOL to the active sites of PDC-3 and PDC-3 Y221H were performed using the Schrodinger software suite. Geometrical optimization and energetic minimization steps were carried out on apo-protein structures of PDC-3 and PDC-3 Y221H proteins by using the Protein Preparation Workflow (73). Ligands CAZ and TOL were prepared with the LigPrep Tool (74). For the docking stage, the Centroid of Workspace Ligand was chosen as the center of the docking grid box and S64 was picked as the Reactive Residue. Reaction type was set as Beta Lactam Addition, and default parameters were selected to run the docking protocol using GLIDE software with the OPLS4 force field. Docking score and ligand interactions with the residues of active sites were recorded.

Enhanced Sampling Molecular Dynamics Simulations

The apo form of the structure of the PDC-3 β -lactamase was used as the starting geometry for the PDC-3 simulations. The missing Ω -loop in the Y221H variant was constructed *in silico* using the ICM loop modelling package (75). The high-throughput molecular dynamics (HTMD) protocol was employed to prepare the simulation systems (76). The protonation states for the side chains were calculated using *proteinprepare* implemented in the Moleculerkit module within the HTMD package. The Amber ff14SB force field parameters were used to describe the protein (77), combined with explicit TIP3P model for water molecules (78). The systems were minimized with 3,000 steps of the steepest descent integrator and equilibrated in the NPT

ensemble for 5 ns. The Langevin thermostat and Berendsen barostat (79) were employed to keep the temperature (300 K) and pressure (1 bar) constant, respectively. A 5 μ s-long production simulation was carried out in the NVT ensemble for all the systems with a time step of 4 fs. All the simulations were run using the ACEMD program (80).

To enhance the sampling, well-tempered metadynamics simulations (81, 82) (WTMetaD) starting from the equilibrated structures of PDC-3 and the Y221H variant were performed at 300 K using the ACEMD program combined with the PLUMED 1.3 plug-in. An integration step of 4 fs was used in WTMetaD. To investigate how the mutation influences the dynamics of the protein, the main chain ϕ and ψ dihedral angles of residue 221 were chosen as the collective variables (CVs) in both PDC-3 and the Y221H variant. The bias was added on the two CVs with a Gaussian width of 0.1 rad and a Gaussian height of 0.5 kJ/mol. Gaussians were deposited every 4 ps, so that the deposition rate was equal to 0.125 kJ/(mol·ps). The bias factor was fixed to 15. After 3 μ s WTMetaD in the NVT ensemble, the free energy reached full convergence (**Figure S8**). The free energy landscape as a function of the two CVs were obtained by integrating the deposited energy bias along the trajectory of WTMetaD simulations. The error on the minima and barriers of the free energy surface was estimated from the largest variation observed in the mono dimensional projections along the collective variables during the last 100 ns of the simulation and amounts to 0.5 kcal/mol. The conformations from each energy minimum were clustered via the root mean square deviation (RMSD) with a cutoff of 0.2 nm. The structures corresponding to the clusters were selected from the WTMetaD trajectories based on the values of the collective variables CV1 and CV2. All structural analysis was conducted via MDtraj (83). The structures extracted from MD simulations were illustrated using Protein Imager (84).

Acknowledgements

Merck & Co., Inc. provided ceftolozane powder for this study.

Research reported herein was supported in part by funds the National Institute of Allergy and Infectious Diseases of the National Institutes of Health under Award Number R01AI063517 to RAB.

The content is solely the responsibility of the authors and does not necessarily represent the official views of the Department of Veterans Affairs or the National Institutes of Health.

Supporting Information

This article contains supporting information. References (85) and (86) are in the supporting information.

Conflict of interest

The authors declare that they have no conflicts of interest with the contents of this article.

Data Availability

Coordinates and structure factors for the all the apo and complex structures have been deposited into Protein Data Bank (PDB) with codes as 8SDL, 8SDN, 8SDR, 8SDS, 8SDT, and 8SDV for apo PDC-3, apo Y221H, LP06: PDC-3, LP06: Y221H, S02030: PDC-3 and S02030: Y221H, respectively.

References

1. Ventola CL. 2015. The antibiotic resistance crisis: part 1: causes and threats. *P T Peer-Rev J Formul Manag* 40:277–283.
2. Bush K, Bradford PA. 2016. β -Lactams and β -Lactamase Inhibitors: An Overview. *Cold Spring Harb Perspect Med* 6:a025247.
3. Giurazza R, Mazza MC, Andini R, Sansone P, Pace MC, Durante-Mangoni E. 2021. Emerging Treatment Options for Multi-Drug-Resistant Bacterial Infections. *Life* 11:519.
4. Lister PD, Wolter DJ, Hanson ND. 2009. Antibacterial-Resistant *Pseudomonas aeruginosa*: Clinical Impact and Complex Regulation of Chromosomally Encoded Resistance Mechanisms. *Clin Microbiol Rev* 22:582–610.
5. Reynolds D, Kollef M. 2021. The Epidemiology and Pathogenesis and Treatment of *Pseudomonas aeruginosa* Infections: An Update. *Drugs* 81:2117–2131.
6. Centers for Disease Control and Prevention. 2019. Antibiotic Resistance Threats in the United States, 2019. Centers for Disease Control and Prevention.
7. Osborn MJ. 1969. Structure and Biosynthesis of the Bacterial Cell Wall. *Annu Rev Biochem* 38:501–538.
8. Cho H, Uehara T, Bernhardt TG. 2014. Beta-Lactam Antibiotics Induce a Lethal Malfunctioning of the Bacterial Cell Wall Synthesis Machinery. *Cell* 159:1300–1311.

9. Bonomo RA. 2017. β -Lactamases: A Focus on Current Challenges. Cold Spring Harb Perspect Med 7:a025239.
10. Bush K. 2013. The ABCD's of β -lactamase nomenclature. J Infect Chemother 19:549–559.
11. Barnes MD, Taracila MA, Rutter JD, Bethel CR, Galdadas I, Hujer AM, Caselli E, Prati F, Dekker JP, Papp-Wallace KM, Haider S, Bonomo RA. 2018. Deciphering the Evolution of Cephalosporin Resistance to Ceftolozane-Tazobactam in *Pseudomonas aeruginosa*. mBio 9.
12. Rodríguez-Martínez J-M, Poirel L, Nordmann P. 2009. Extended-spectrum cephalosporinases in *Pseudomonas aeruginosa*. Antimicrob Agents Chemother 53:1766–1771.
13. Mack AR, Barnes MD, Taracila MA, Hujer AM, Hujer KM, Cabot G, Feldgarden M, Haft DH, Klimke W, van den Akker F, Vila AJ, Smania A, Haider S, Papp-Wallace KM, Bradford PA, Rossolini GM, Docquier J-D, Frère J-M, Galleni M, Hanson ND, Oliver A, Plésiat P, Poirel L, Nordmann P, Palzkill TG, Jacoby GA, Bush K, Bonomo RA. 2019. A standard numbering scheme for class C β -lactamases. Antimicrob Agents Chemother <https://doi.org/10.1128/AAC.01841-19>.
14. Drawz SM, Taracila M, Caselli E, Prati F, Bonomo RA. 2011. Exploring sequence requirements for C₃/C₄ carboxylate recognition in the *Pseudomonas aeruginosa* cephalosporinase: Insights into plasticity of the AmpC β -lactamase. Protein Sci Publ Protein Soc 20:941–958.
15. Jacoby GA. 2009. AmpC β -lactamases. Clin Microbiol Rev 22:161–182.

16. Berrazeg M, Jeannot K, Enguéné VYN, Broutin I, Loeffert S, Fournier D, Plésiat P. 2015. Mutations in β -lactamase AmpC increase resistance of *Pseudomonas aeruginosa* isolates to antipseudomonal cephalosporins. *Antimicrob Agents Chemother* 59:6248–6255.
17. López-Causapé C, Cabot G, del Barrio-Tofiño E, Oliver A. 2018. The Versatile Mutational Resistome of *Pseudomonas aeruginosa*. *Front Microbiol* 9:685.
18. Torrens G, Hernández SB, Ayala JA, Moya B, Juan C, Cava F, Oliver A. 2019. Regulation of AmpC-Driven β -Lactam Resistance in *Pseudomonas aeruginosa*: Different Pathways, Different Signaling. *mSystems* 4:e00524-19.
19. Juan C, Moyá B, Pérez JL, Oliver A. 2006. Stepwise upregulation of the *Pseudomonas aeruginosa* chromosomal cephalosporinase conferring high-level β -lactam resistance involves three AmpD homologues. *Antimicrob Agents Chemother* 50:1780–1787.
20. Moya B, Dötsch A, Juan C, Blázquez J, Zamorano L, Haussler S, Oliver A. 2009. β -lactam resistance response triggered by inactivation of a nonessential penicillin-binding protein. *PLoS Pathog* 5:e1000353.
21. Toda A, Ohki H, Yamanaka T, Murano K, Okuda S, Kawabata K, Hatano K, Matsuda K, Misumi K, Itoh K, Satoh K, Inoue S. 2008. Synthesis and SAR of novel parenteral anti-pseudomonal cephalosporins: Discovery of FR264205. *Bioorg Med Chem Lett* 18:4849–4852.
22. Takeda S, Ishii Y, Hatano K, Tateda K, Yamaguchi K. 2007. Stability of FR264205 against AmpC β -lactamase of *Pseudomonas aeruginosa*. *Int J Antimicrob Agents* 30:443–445.

23. Papp-Wallace KM, Mack AR, Taracila MA, Bonomo RA. 2020. Resistance to Novel β -Lactam- β -Lactamase Inhibitor Combinations: The “Price of Progress.” *Infect Dis Clin North Am* 34:773–819.
24. Karlowsky JA, Lob SH, DeRyke CA, Hilbert DW, Wong MT, Young K, Siddiqui F, Motyl MR, Sahn DF. 2022. In Vitro Activity of Ceftolozane-Tazobactam, Imipenem-Relebactam, Ceftazidime-Avibactam, and Comparators against *Pseudomonas aeruginosa* Isolates Collected in United States Hospitals According to Results from the SMART Surveillance Program, 2018 to 2020. *Antimicrob Agents Chemother* 66:e00189-22.
25. Drawz SM, Bonomo RA. 2010. Three Decades of β -Lactamase Inhibitors. *Clin Microbiol Rev* 23:160–201.
26. López-Argüello S, Montaner M, Oliver A, Moya B. 2021. Molecular Basis of AmpC β -Lactamase Induction by Avibactam in *Pseudomonas aeruginosa*: PBP Occupancy, Live Cell Binding Dynamics and Impact on Resistant Clinical Isolates Harboring PDC-X Variants. *Int J Mol Sci* 22:3051.
27. Ruedas-López A, Alonso-García I, Lasarte-Monterrubio C, Guijarro-Sánchez P, Gato E, Vázquez-Ucha JC, Vallejo JA, Fraile-Ribot PA, Fernández-Pérez B, Velasco D, Gutiérrez-Urbón JM, Oviaño M, Beceiro A, González-Bello C, Oliver A, Arca-Suárez J, Bou G. 2022. Selection of AmpC β -Lactamase Variants and Metallo- β -Lactamases Leading to Ceftolozane/Tazobactam and Ceftazidime/Avibactam Resistance during Treatment of MDR/XDR *Pseudomonas aeruginosa* Infections. *Antimicrob Agents Chemother* 66:e02067-21.

28. Fournier D, Carrière R, Bour M, Grisot E, Triponney P, Muller C, Lemoine J, Jeannot K, Plésiat P, the GERPA Study Group. 2021. Mechanisms of Resistance to Ceftolozane/Tazobactam in *Pseudomonas aeruginosa*: Results of the GERPA Multicenter Study. *Antimicrob Agents Chemother* 65:e01117-20.
29. Barnes MD, Bethel CR, Alsop J, Becka SA, Rutter JD, Papp-Wallace KM, Bonomo RA. 2018. Inactivation of the *Pseudomonas*-Derived Cephalosporinase-3 (PDC-3) by Relebactam. *Antimicrob Agents Chemother* 62.
30. Lomovskaya O, Tsivkovski R, Nelson K, Rubio-Aparicio D, Sun D, Totrov M, Dudley MN. 2020. Spectrum of Beta-Lactamase Inhibition by the Cyclic Boronate QPX7728, an Ultrabroad-Spectrum Beta-Lactamase Inhibitor of Serine and Metallo-Beta-Lactamases: Enhancement of Activity of Multiple Antibiotics against Isogenic Strains Expressing Single Beta-Lactamases. *Antimicrob Agents Chemother* 64:e00212-20.
31. Cahill ST, Tyrrell JM, Navratilova IH, Calvopiña K, Robinson SW, Lohans CT, McDonough MA, Cain R, Fishwick CWG, Avison MB, Walsh TR, Schofield CJ, Brem J. 2019. Studies on the inhibition of AmpC and other β -lactamases by cyclic boronates. *Biochim Biophys Acta BBA - Gen Subj* 1863:742–748.
32. Lahiri SD, Mangani S, Durand-Reville T, Benvenuti M, Luca FD, Sanyal G, Docquier J-D. 2013. Structural Insight into Potent Broad-Spectrum Inhibition with Reversible Recyclization Mechanism: Avibactam in Complex with CTX-M-15 and *Pseudomonas aeruginosa* AmpC β -Lactamases. *Antimicrob Agents Chemother* 57:2496–2505.

33. Naas T, Oueslati S, Bonnin RA, Dabos ML, Zavala A, Dortet L, Retailleau P, Iorga BI. 2017. Beta-lactamase database (BLDB) – structure and function. *J Enzyme Inhib Med Chem* 32:917–919.
34. Clinical & Laboratory Standards Institute. 2022. M100: Performance Standards for Antimicrobial Susceptibility Testing, 32nd Edition, 32nd ed. <https://clsi.org/standards/products/microbiology/documents/m100/>. Retrieved 21 November 2022.
35. Cabot G, Kim K, Mark BL, Oliver A, Khajehpour M. 2023. Biochemical Insights into Imipenem Collateral Susceptibility Driven by ampC Mutations Conferring Ceftolozane/Tazobactam Resistance in *Pseudomonas aeruginosa*. *Antimicrob Agents Chemother* 67:e0140922.
36. Fersht A. 1985. *Enzyme Structure and Mechanism* Second Edition. W. H. Freeman, New York.
37. Papp-Wallace KM, Taracila M, Wallace CJ, Hujer KM, Bethel CR, Hornick JM, Bonomo RA. 2010. Elucidating the role of Trp105 in the KPC-2 β -lactamase. *Protein Sci Publ Protein Soc* 19:1714–1727.
38. Papp-Wallace KM, Bethel CR, Distler AM, Kasuboski C, Taracila M, Bonomo RA. 2010. Inhibitor Resistance in the KPC-2 β -Lactamase, a Preeminent Property of This Class A β -Lactamase. *Antimicrob Agents Chemother* 54:890–897.
39. Cabot G, Bruchmann S, Mulet X, Zamorano L, Moyà B, Juan C, Haussler S, Oliver A. 2014. *Pseudomonas aeruginosa* ceftolozane-tazobactam resistance development requires

multiple Mutations leading to overexpression and structural modification of AmpC.

Antimicrob Agents Chemother 58:3091–3099.

40. Fraile-Ribot PA, Cabot G, Mulet X, Periañez L, Martín-Pena ML, Juan C, Pérez JL, Oliver A. 2018. Mechanisms leading to *in vivo* ceftolozane/tazobactam resistance development during the treatment of infections caused by MDR *Pseudomonas aeruginosa*. J Antimicrob Chemother 73:658–663.
41. Stojanoski V, Chow D-C, Hu L, Sankaran B, Gilbert HF, Prasad BVV, Palzkill T. 2015. A Triple Mutant in the Ω -loop of TEM-1 β -Lactamase Changes the Substrate Profile via a Large Conformational Change and an Altered General Base for Catalysis. J Biol Chem 290:10382–10394.
42. Beadle BM, MCGovern SL, Patera A, Shoichet BK. 1999. Functional analyses of AmpC β -lactamase through differential stability. Protein Sci 8:1816–1824.
43. Mehta SC, Rice K, Palzkill T. 2015. Natural Variants of the KPC-2 Carbapenemase have Evolved Increased Catalytic Efficiency for Ceftazidime Hydrolysis at the Cost of Enzyme Stability. PLOS Pathog 11:e1004949.
44. Vihinen M. 1987. Relationship of protein flexibility to thermostability. Protein Eng Des Sel 1:477–480.
45. Slater CL, Winogrodzki J, Fraile-Ribot PA, Oliver A, Khajehpour M, Mark BL. 2020. Adding Insult to Injury: Mechanistic Basis for How AmpC Mutations Allow *Pseudomonas aeruginosa* To Accelerate Cephalosporin Hydrolysis and Evade Avibactam. Antimicrob Agents Chemother 64:e00894-20.

46. Barnes MD, Taracila MA, Good CE, Bajaksouzian S, Rojas LJ, van Duin D, Kreiswirth BN, Jacobs MR, Haldimann A, Papp-Wallace KM, Bonomo RA. 2019. Nacubactam Enhances Meropenem Activity against Carbapenem-Resistant *Klebsiella pneumoniae* Producing KPC. *Antimicrob Agents Chemother* 63:e00432-19.
47. Powers RA, Caselli E, Focia PJ, Prati F, Shoichet BK. 2001. Structures of Ceftazidime and Its Transition-State Analogue in Complex with AmpC β -Lactamase: Implications for Resistance Mutations and Inhibitor Design,. *Biochemistry* 40:9207–9214.
48. Nukaga M, Haruta S, Tanimoto K, Kogure K, Taniguchi K, Tamaki M, Sawai T. 1995. Molecular Evolution of a Class C β -Lactamase Extending Its Substrate Specificity (*). *J Biol Chem* 270:5729–5735.
49. Crichlow GV, Kuzin AP, Nukaga M, Mayama K, Sawai T, Knox JR. 1999. Structure of the Extended-Spectrum Class C β -Lactamase of *Enterobacter cloacae* GC1, a Natural Mutant with a Tandem Tripeptide Insertion,. *Biochemistry* 38:10256–10261.
50. Curtis BN, Smolen KA, Barlow SJ, Caselli E, Prati F, Taracila MA, Bonomo RA, Wallar BJ, Powers RA. 2020. Structural Insights into Inhibition of the Acinetobacter-Derived Cephalosporinase ADC-7 by Ceftazidime and Its Boronic Acid Transition State Analog. *Antimicrob Agents Chemother* 64:e01183-20.
51. Zavala A, Retailleau P, Elisée E, Iorga BI, Naas T. 2019. Genetic, Biochemical, and Structural Characterization of CMY-136 β -Lactamase, a Peculiar CMY-2 Variant. *ACS Infect Dis* 5:528–538.

52. Lefurgy ST, Caselli E, Taracila MA, Malashkevich VN, Biju B, Papp-Wallace KM, Bonanno JB, Prati F, Almo SC, Bonomo RA. 2020. Structures of FOX-4 Cephamycinase in Complex with Transition-State Analog Inhibitors. *Biomolecules* 10:671.
53. Powers RA, Swanson HC, Taracila MA, Florek NW, Romagnoli C, Caselli E, Prati F, Bonomo RA, Wallar BJ. 2014. Biochemical and Structural Analysis of Inhibitors Targeting the ADC-7 Cephalosporinase of *Acinetobacter baumannii*. *Biochemistry* 53:7670–7679.
54. Ishikawa T, Furukawa N, Caselli E, Prati F, Taracila MA, Bethel CR, Ishii Y, Shimizu-Ibuka A, Bonomo RA. 2021. Insights Into the Inhibition of MOX-1 β -Lactamase by S02030, a Boronic Acid Transition State Inhibitor. *Front Microbiol* 12:720036.
55. Pantsar T, Poso A. 2018. Binding Affinity via Docking: Fact and Fiction. *Molecules* 23:1899.
56. Alsenani TA, Viviani SL, Kumar V, Taracila MA, Bethel CR, Barnes MD, Papp-Wallace KM, Shields RK, Nguyen MH, Clancy CJ, Bonomo RA, van den Akker F. 2022. Structural Characterization of the D179N and D179Y Variants of KPC-2 β -Lactamase: Ω -Loop Destabilization as a Mechanism of Resistance to Ceftazidime-Avibactam. *Antimicrob Agents Chemother* 66:e02414-21.
57. Liao S-M, Du Q-S, Meng J-Z, Pang Z-W, Huang R-B. 2013. The multiple roles of histidine in protein interactions. *Chem Cent J* 7:44.
58. Rojas LJ, Taracila MA, Papp-Wallace KM, Bethel CR, Caselli E, Romagnoli C, Winkler ML, Spellberg B, Prati F, Bonomo RA. 2016. Boronic Acid Transition State Inhibitors

Active against KPC and Other Class A β -Lactamases: Structure-Activity Relationships as a Guide to Inhibitor Design. *Antimicrob Agents Chemother* 60:1751–1759.

59. Nguyen NQ, Krishnan NP, Rojas LJ, Prati F, Caselli E, Romagnoli C, Bonomo RA, van den Akker F. 2016. Crystal Structures of KPC-2 and SHV-1 β -Lactamases in Complex with the Boronic Acid Transition State Analog S02030. *Antimicrob Agents Chemother* 60:1760–1766.
60. Colque CA, albarracín Orio AG, Tomatis PE, Dotta G, Moreno DM, Hedemann LG, Hickman RA, Sommer LM, Feliziani S, Moyano AJ, Bonomo RA, K. Johansen H, Molin S, Vila AJ, Smania AM. 2022. Longitudinal Evolution of the *Pseudomonas*-Derived Cephalosporinase (PDC) Structure and Activity in a Cystic Fibrosis Patient Treated with β -Lactams. *mBio* 13:e01663-22.
61. Kurz SG, Hazra S, Bethel CR, Romagnoli C, Caselli E, Prati F, Blanchard JS, Bonomo RA. 2015. Inhibiting the β -Lactamase of *Mycobacterium tuberculosis* (Mtb) with Novel Boronic Acid Transition-State Inhibitors (BATSIs). *ACS Infect Dis* 1:234–242.
62. Levitt PS, Papp-Wallace KM, Taracila MA, Hujer AM, Winkler ML, Smith KM, Xu Y, Harris ME, Bonomo RA. 2012. Exploring the role of a conserved class a residue in the Ω -loop of KPC-2 β -lactamase: a mechanism for ceftazidime hydrolysis. *J Biol Chem* jbc.M112.348540.
63. Greenfield NJ. 2006. Using circular dichroism collected as a function of temperature to determine the thermodynamics of protein unfolding and binding interactions. 6. *Nat Protoc* 1:2527–2535.

64. Bouza AA, Swanson HC, Smolen KA, VanDine AL, Taracila MA, Romagnoli C, Caselli E, Prati F, Bonomo RA, Powers RA, Wallar BJ. 2018. Structure-Based Analysis of Boronic Acids as Inhibitors of Acinetobacter-Derived Cephalosporinase-7, a Unique Class C β -Lactamase. *ACS Infect Dis* 4:325–336.
65. Becktel WJ, Schellman JA. 1987. Protein stability curves. *Biopolymers* 26:1859–1877.
66. Kabsch W. 2010. *XDS*. *Acta Crystallogr D Biol Crystallogr* 66:125–132.
67. Minor W, Cymborowski M, Otwinowski Z, Chruszcz M. 2006. *HKL* -3000: the integration of data reduction and structure solution – from diffraction images to an initial model in minutes. *Acta Crystallogr D Biol Crystallogr* 62:859–866.
68. Vagin A, Teplyakov A. 2010. Molecular replacement with *MOLREP*. *Acta Crystallogr D Biol Crystallogr* 66:22–25.
69. Chen H, Blizzard TA, Kim S, Wu J, Young K, Park Y-W, Ogawa AM, Raghoobar S, Painter RE, Wisniewski D, Hairston N, Fitzgerald P, Sharma N, Scapin G, Lu J, Hermes J, Hammond ML. 2011. Side chain SAR of bicyclic β -lactamase inhibitors (BLIs). 2. N-Alkylated and open chain analogs of MK-8712. *Bioorg Med Chem Lett* 21:4267–4270.
70. Murshudov GN, Skubák P, Lebedev AA, Pannu NS, Steiner RA, Nicholls RA, Winn MD, Long F, Vagin AA. 2011. *REFMAC 5* for the refinement of macromolecular crystal structures. *Acta Crystallogr D Biol Crystallogr* 67:355–367.
71. Emsley P, Cowtan K. 2004. *Coot* : model-building tools for molecular graphics. *Acta Crystallogr D Biol Crystallogr* 60:2126–2132.

72. Long F, Nicholls RA, Emsley P, Gražulis S, Merkys A, Vaitkus A, Murshudov GN. 2017. *AceDRG*: a stereochemical description generator for ligands. *Acta Crystallogr Sect Struct Biol* 73:112–122.
73. Schrödinger, LLC. 2021. Schrödinger Release 2021-4: Protein Preparation Wizard; Epik; Impact; Prime. New York, NY, USA.
74. Schrödinger, LLC. 2021. Schrödinger Release 2022-4: LigPrep. New York, NY, USA.
75. Abagyan R, Totrov M, Kuznetsov D. 1994. ICM - A new method for protein modeling and design: Applications to docking and structure prediction from the distorted native conformation. *J Comput Chem* 15:488–506.
76. Doerr S, Harvey MJ, Noé F, De Fabritiis G. 2016. HTMD: High-Throughput Molecular Dynamics for Molecular Discovery. *J Chem Theory Comput* 12:1845–1852.
77. Case DA, Cheatham TE, Darden T, Gohlke H, Luo R, Merz KM, Onufriev A, Simmerling C, Wang B, Woods RJ. 2005. The Amber biomolecular simulation programs. *J Comput Chem* 26:1668–1688.
78. Price DJ, Brooks CL. 2004. A modified TIP3P water potential for simulation with Ewald summation. *J Chem Phys* 121:10096–10103.
79. Berendsen HJC, Postma JPM, van Gunsteren WF, DiNola A, Haak JR. 1984. Molecular dynamics with coupling to an external bath. *J Chem Phys* 81:3684–3690.
80. Harvey MJ, Giupponi G, Fabritiis GD. 2009. ACEMD: Accelerating Biomolecular Dynamics in the Microsecond Time Scale. *J Chem Theory Comput* 5:1632–1639.

81. Bonomi M, Barducci A, Parrinello M. 2009. Reconstructing the equilibrium Boltzmann distribution from well-tempered metadynamics. *J Comput Chem* 30:1615–1621.
82. Laio A, Gervasio FL. 2008. Metadynamics: a method to simulate rare events and reconstruct the free energy in biophysics, chemistry and material science. *Rep Prog Phys* 71:126601.
83. McGibbon RT, Beauchamp KA, Harrigan MP, Klein C, Swails JM, Hernández CX, Schwantes CR, Wang L-P, Lane TJ, Pande VS. 2015. MDTraj: A Modern Open Library for the Analysis of Molecular Dynamics Trajectories. *Biophys J* 109:1528–1532.
84. Tomasello G, Armenia I, Molla G. 2020. The Protein Imager: a full-featured online molecular viewer interface with server-side HQ-rendering capabilities. *Bioinformatics* 36:2909–2911.
85. Millipore Sigma. Post Translational Modification.
<https://www.sigmaaldrich.com/US/en/technical-documents/technical-article/protein-biology/protein-labeling-and-modification/post-translational-modification>. Retrieved 4 April 2023.
86. Badarau A, Llinás A, Laws AP, Damblon C, Page MI. 2005. Inhibitors of Metallo- β -lactamase Generated from β -Lactam Antibiotics. *Biochemistry* 44:8578–8589.

Abbreviations

- PDC, *Pseudomonas*-derived cephalosporinase
- CAZ, ceftazidime
- TOL, ceftolozane
- NCF, nitrocefin
- AVI, avibactam
- TAZO, tazobactam
- MDR, multi-drug resistant

Tables

Table 1: Kinetic profiles of PDC-3, E219K, and Y221H with CAZ, TOL, and NCF. Data was collected spectrophotometrically and is presented as the mean \pm standard deviation of three independent replicates. Less-than (<) and greater-than (>) values are estimated based on the parameters of the experiments.

Substrate	PDC-3			PDC-3 E219K			PDC-3 Y221H		
	K_M (μM)	k_{cat} (s^{-1})	k_{cat}/K_M ($\mu M^{-1} s^{-1}$)	K_M (μM)	k_{cat} (s^{-1})	k_{cat}/K_M ($\mu M^{-1} s^{-1}$)	K_M (μM)	k_{cat} (s^{-1})	k_{cat}/K_M ($\mu M^{-1} s^{-1}$)
Nitrocefin	28.9 \pm 3.9	875.4 \pm 119.6	30.3 \pm 2.0	16.7 \pm 0.4	76.0 \pm 2.8	4.6 \pm 0.2	26.2 \pm 2.1	375.4 \pm 28.1	14.3 \pm 0.08
Ceftazidime	38.9 \pm 1.3	< 0.1	< 0.0026	538.1 \pm 80.0	5.9 \pm 0.3	0.011 \pm 0.001	756.5 \pm 23.0	2.3 \pm 0.2	0.0031 \pm 0.0003
Ceftolozane	> 50	< 0.01	< 0.0002	407.3 \pm 24.7	5.6 \pm 0.7	0.014 \pm 0.0005	411.3 \pm 29.5	2.6 \pm 0.1	0.0062 \pm 0.0004

Table 2. Masses of PDC-3, PDC-3 E219K, and PDC-3 Y221H, both unbound and in their respective acyl-enzyme complexes, with and without the addition of a water molecule. A green check mark (✓) indicates a mass that was observed. The R2 group is eliminated from both cephalosporins in the collapse of the transition state leading to the formation of the acyl-enzyme complex. The variable Met residue is the result of cloning and protein production and does not impact β -lactamase activity. CAZ, ceftazidime; TOL, ceftolozane.

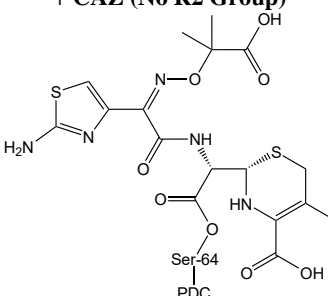
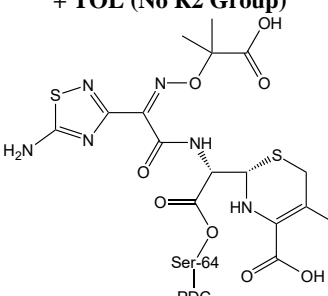
Change in Structure	Change in Mass	WT	E219K	Y221H
		✓ 40,648	✓ 40,647	✓ 40,622
+ Methionine	+ 131	✓ 40,779	✓ 40,778	✓ 40,753
+ CAZ (No R2 Group)		✓ 41,119	41,118	41,093
+ CAZ (No R2 Group) + Modification		+ 487	✓ 41,135	✓ 41,134
+ Methionine + CAZ (No R2 Group)	+ 602	41,250	41,249	41,224
+ Methionine + CAZ (No R2 Group) + Modification	+ 618	✓ 41,266	41,265	41,240
+ TOL (No R2 Group)		41,120	41,119	41,094
+ TOL (No R2 Group) + Modification		+ 488	✓ 41,136	✓ 41,135
+ Methionine + TOL (No R2 Group)	+ 603	41,251	41,250	41,225
+ Methionine + TOL (No R2 Group) + Modification	+ 619	✓ 41,267	41,266	41,241

Table 3. Changes in enzyme T_m on addition of inhibitor. Values were determined using circular dichroism and are presented in °C, accurate to $\pm 1^\circ\text{C}$, for T_m and in $\text{kJ K}^{-1} \text{mol}^{-1}$ for $\Delta\Delta G_u$. Positive values indicate stabilization on binding and negative values destabilization.

Enzyme	Apo	AVI		LP06		S02030		TAZO	
	ΔT_m	ΔT_m	$\Delta\Delta G_u$	ΔT_m	$\Delta\Delta G_u$	ΔT_m	$\Delta\Delta G_u$	ΔT_m	$\Delta\Delta G_u$
PDC-3	0	-0.8	-1.1	5.5	8.0	4.9	7.2	0.8	1.1
PDC-3 E219K	0	1.4	2.1	2.5	3.3	2.1	2.7	1.1	1.4
PDC-3 Y221H	0	-0.9	-1.4	3.8	6.0	2.6	4.0	0.3	0.5

Table 4. Inhibition kinetics with PDC-3, E219K, and Y221H. Fifty percent inhibitory concentration (IC_{50}) values were determined spectrophotometrically following a five-minute preincubation of inhibitor and enzyme, corrected for competition of the reporter substrate, and are provided in nM as the mean \pm standard deviation of three independent replicates. AVI, avibactam; TAZO, tazobactam.

Inhibitor	PDC-3 IC_{50}	PDC-3 E219K IC_{50}	PDC-3 Y221H IC_{50}
LP06	4.6 \pm 0.6	144.4 \pm 13.9	18.2 \pm 6.0
S02030	8.5 \pm 1.8	53.1 \pm 3.7	116.8 \pm 18.0
AVI	10.7 \pm 0.5	20.0 \pm 2.5	24.8 \pm 0.8
TAZO	180.3 \pm 15.2	105.4 \pm 24.9	30.3 \pm 0.6

Table 5. X-ray diffraction data collection and crystallographic refinement statistics for the PDC-3 and mutant Y221H proteins & their complexes with ligands LP06 and S02030.

Parameters	Apo PDC-3	Apo Y221H	LP-06:PDC-3	LP-06:Y221H	S02030:PDC-3	S02030:Y221H
Indexing and scaling						
Wavelength (Å)	0.920097	0.97946	0.97933	0.97935	0.97946	0.97935
Resolution range (Å)	37.96 – 1.75 (1.78-1.75)	50-2.10 (2.18- 2.10)	27.99-1.35 (1.38- 1.35)	28.02-1.63 (1.67- 1.63)	37.94-1.38 (1.40- 1.38)	29.6-1.42 (1.46- 1.42)
Space group	P2 ₁ 2 ₁ 2 ₁	P2 ₁ 2 ₁ 2 ₁	P2 ₁ 2 ₁ 2 ₁	P2 ₁ 2 ₁ 2 ₁	P2 ₁ 2 ₁ 2 ₁	P2 ₁ 2 ₁ 2 ₁
Unit cell (Å, °)	44.87 70.99 106.27, 90 90 90	44.83 71.31 106.73 90 90 90	44.83 71.67 106.73, 90 90 90	45.10 71.40 105.80, 90 90 90	44.73 71.60 106.62, 90 90 90	44.67 71.77 104.78, 90 90 90
Unique reflections	34,712 (1,717)	20,364 (1,977)	76,325 (5,339)	43,613 (3,117)	70,912 (3,259)	64,139 (4,477)
Multiplicity	12.8 (12.7)	6.5 (6.8)	6.6 (5.4)	13.1 (12.9)	6.2 (4.7)	13.2 (12.0)
Completeness (%)	99.2 (99.8)	99.8 (99.8)	99.5 (93.7)	99.8 (97.8)	99.4 (93.5)	99.6 (95.2)
Mean I/sigma (I)	33.37 (6.39)	9.42 (6.7)	14.8 (3.0)	21.10 (3.40)	15.3 (1.9)	20.6 (3.0)
CC _{1/2}	0.996 (0.960)	0.923 (0.972)	0.998 (0.896)	0.999 (0.897)	0.998 (0.712)	0.999 (0.883)
R-merge	0.093 (0.81)	0.15 (0.177)	0.134 (0.626)	0.097 (0.806)	0.056 (0.632)	0.076 (0.704)
Refinement						
Resolution refinement (Å)	37.96 – 1.75	35.61-2.1	28.01-1.35	28.04-1.63	37.97-1.38	29.62-1.42
Reflections used in refinement	32,945	19,312	72326	41300	67,236	60,901
Reflections used for R-free	1,604	987	3919	2246	3608	3163
R-work	0.155	0.1791	0.1291	0.1544	0.1266	0.1454
R-free	0.197	0.2398	0.1611	0.1879	0.1642	0.1627
Number of non-hydrogen atoms	3168	3033	3510	3430	3426	3483
RMS(bonds, Å)	0.012	0.008	0.010	0.008	0.008	0.010
RMS(angles, °)	1.74	1.53	1.604	1.681	1.520	1.65
Overall average B-factor (Å ²)	19.77	15.83	10.80	17.24	13.40	15.10
Ramachandran Plot						
Residues in most favored regions (%)	100	100	100	100	100	100
No. of outliers (%)	0 (0)	0 (0)	1 (0)	1 (0)	1 (0)	0 (0)

Statistics for the highest-resolution shell are shown in parentheses.

Figure Legends

Figure 1. Chemical structures of A) the oxyimino cephalosporins CAZ and TOL, B) the monobactam ATM, and C) the β -lactamase inhibitors AVI, TAZO, LP06, and S02030. The R1 and R2 sidechains in cephalosporins (or equivalent positions in other compounds) are depicted in red and blue, respectively. CAZ, ceftazidime; TOL, ceftolozane; AVI, avibactam; TAZO, tazobactam.

Figure 2. Electrospray ionization mass spectrometry (ESI-MS) of purified PDC-3, PDC-3 E219K, and PDC-3 Y221H incubated with CAZ for 15 s at a 1:50 molar ratio. The presence or absence of Methionine (Met; 131 Da) is an artifact of the protein production process. Mass accuracy is ± 5 Da.

Figure 3A. Circular dichroism spectrophotometry (CD) melting curves of PDC-3, PDC-3 E219K, and PDC-3 Y221H. Data collected at 208 nm and presented as a normalized fraction of the protein folded.

Figure 3B. Differential scanning fluorimetry (DSF) assay for binding of the ligands LP06 and S02030 to proteins PDC-3 and PDC-3 Y221H. Experiments were performed in duplicate and DMSO controls were included.

Figure 4. Crystal structures of PDC-3 and PDC-3 Y221H. A, active site region of PDC-3. The catalytic S64 and key flanking residues are shown. Y150 was observed in two conformations (1 and 2). The isopropyl alcohol (IPA) observed in the active site is shown with green carbon atoms and hydrogen bonds are shown as dashed lines. The hydrogen bonding network involving residue Y221 and Ω -loop D217 and two water molecules is shown in dashed lines (involves waters W#1 and W#2). B, same as A but for PDC-3 Y221Y variant. The end-points of the disordered Ω -loop

are indicated by spheres and their residue (G204 and P213) are labeled. Residue D217 is observed in two conformations. C, close-up view of superimposition of PDC-3 and PDC-3 Y221H structures. The IPA observed in the active sites are labeled. The site of the Y221H variation is labeled bold, and the conformational rotation between the Y221 and H221 side chains is shown via a curved dashed arrow. The PDC-3 Ω -loop residues missing in the PDC-3 Y221H structure are labeled ' Ω -loop'.

Figure 5. Crystal structure of PDC-3 LP06 complex structure. A, Unbiased omit $|F_o| - |F_c|$ electron density map in which LP06 had been removed prior to 10 cycles of refinement and subsequent map calculation (contoured at the 3σ level). B, same as A but view rotated about 90° . C, interactions of LP06 in the PDC-3 active site. Hydrogen bonds are indicated by dashed lines. D, same as C but view rotated about 90° .

Figure 6. Crystal structure of PDC-3 Y221H LP06 complex structure. A-D, panels same as Figure 5.

Figure 7. Superimposition of LP06 complexes of PDC-3 and FOX-4 β -lactamase. PDC-3 (colored as in Figure 5) and FOX-4 (cyan) with LP06 (in ball-and-stick model). Active site hydrogen bonds of LP06 are indicated by black and gray dashed lines for PDC-3 and FOX-4 complexes, respectively. Active site amino acid differences between PDC-3 and FOX-4 are indicated (i.e., A292S, L293F, and N320G).

Figure 8. Crystal structure of PDC-3 S02030 complex structure. A, Unbiased omit $|F_o| - |F_c|$ electron density map in which S02030 had been removed prior to 10 cycles of refinement and subsequent map calculation (contoured at the 3σ level). B, same as A but view rotated about 90° .

C, interactions of S02030 in the PDC-3 active site. Hydrogen bonds are indicated by dashed lines.

D, same as C but view rotated about 90°.

Figure 9. Crystal structure of PDC-3 Y221H S02030 complex structure. A-D, panels same as Figure 8.

Figure 10. Free energy landscape and conformational clustering. Free energy surface (FES) plots for PDC-3 and the Y221H variant were generated as a function of main chain Φ and ψ backbone dihedral angles. Two distinct energy minima (labelled A and B) were identified. The conformations of Y221 and H221 extracted from the basins have been illustrated.